www.acsnano.org

# Substrate Partitioning into Protein Macromolecular Frameworks for Enhanced Catalytic Turnover

Ekaterina Selivanovitch, Masaki Uchida, Byeongdu Lee, and Trevor Douglas\*



Downloaded via INDIANA UNIV BLOOMINGTON on September 23, 2021 at 17:36:46 (UTC). See https://pubs.acs.org/sharingguidelines for options on how to legitimately share published articles.

Cite This: https://doi.org/10.1021/acsnano.1c05004



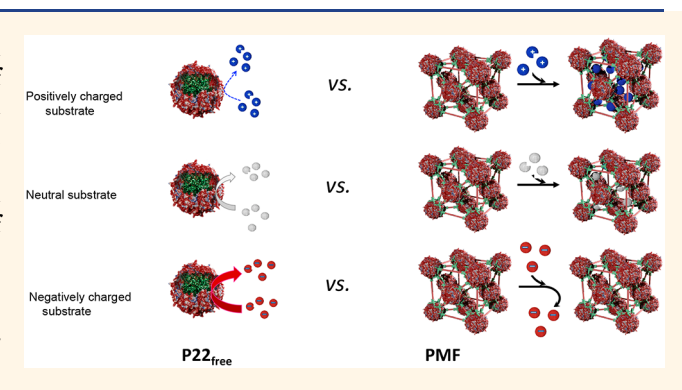
**ACCESS** 

Metrics & More

Article Recommendations

Supporting Information

ABSTRACT: Spatial partitioning of chemical processes is an important attribute of many biological systems, the effect of which is reflected in the high efficiency of enzymes found within otherwise chaotic cellular environments. Barriers, often provided through the formation of compartments or phase segregation, gate the access of macromolecules and small molecules within the cell and provide an added level of metabolic control. Taking inspiration from nature, we have designed virus-like particles (VLPs) as nanoreactor compartments that sequester enzyme catalysts and have used these as building blocks to construct 3D protein macromolecular framework (PMF) materials, which are structurally characterized using small-angle X-ray scattering (SAXS). The highly



charged PMFs form a separate phase in suspension, and by tuning the ionic strength, we show positively charged molecules preferentially partition into the PMF, while negatively charged molecules are excluded. This molecular partitioning was exploited to tune the catalytic activity of enzymes enclosed within the individual particles in the PMF, the results of which showed that positively charged substrates had turnover rates that were 8500× faster than their negatively charged counterparts. Moreover, the catalytic PMF led to cooperative behavior resulting in charge dependent trends opposite to those observed with individual P22 nanoreactor particles.

**KEYWORDS:** protein macromolecular framework (PMF), virus-like particle (VLP), heterogeneous catalyst, catalytic material, partition coefficient, emergent property

upramolecular assemblies found in nature often exhibit collective behaviors that are not evident in their individual building blocks. As an example, the assembly of an infectious virus cannot be easily predicted from studying the individual macromolecular components.<sup>2</sup> Hierarchically assembled virus particles can also exhibit new properties, such as Iridovirus particles that form intracellular photonic crystalline arrays resulting in an iridescence of the infected organism.3 Hierarchical assemblies and the collective properties that arise from them often contribute to the efficiency of biological systems, allowing simple organisms to carry out complex tasks.<sup>4-7</sup> A major goal for biomimetic materials has been to use bottom-up approaches to design and construct functional hierarchical assemblies with new properties and functions.<sup>8-10</sup> Toward the realization of this, both 2-D and 3-D lattices have been designed with tunable physical and chemical features, such as modulating the intercomponent distances, responding to external stimuli, and demonstrating self-healing properties. <sup>11–17</sup> Higher-order assemblies found in biology also provide enzymes optimal environments in which to perform important transformations and have inspired strategies for improving catalyst selectivity and efficiency in synthetically derived biomimetic materials. <sup>18</sup> Metal organic frameworks (MOFs) and polymer hydrogels are additional examples of highly porous synthetic systems which have been shown to behave as highly efficient biomimetic catalysts. <sup>19–22</sup>

Much like infectious viruses, virus-like particles (VLPs) hierarchically self-assemble from protein building blocks and have been repurposed by using their interior cavities, intended for the encapsulation and protection of the viral genome, for

Received: June 11, 2021 Accepted: August 27, 2021



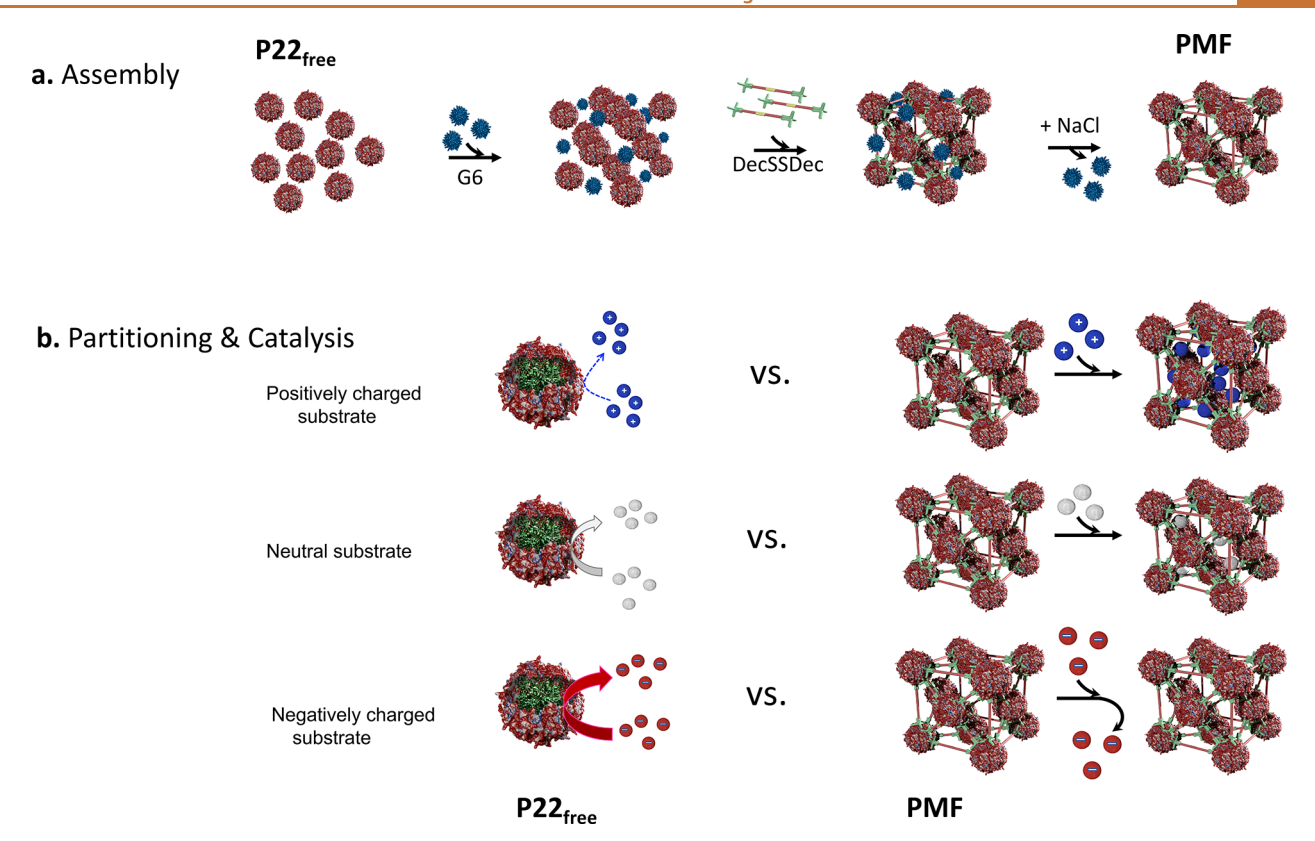


Figure 1. Overall schematic. (a) The higher-order assembly was carried out by first using G6 to template the assembly of  $P22_{free}$  particles into an fcc lattice. A cementing protein (DecSSDec) was added to stabilize and lock the lattice into place. In order to remove G6, the ionic strength was increased, and the remaining protein assembly was washed several times yielding a protein macromolecular framework (PMF) as the final product. (b) Shows positive, neutral, and negatively charged substrates interacting with  $P22_{free}$  and the PMF. The enzyme filled P22 VLPs as individual particles (P22 $_{free}$ ) do not show activity with positive substrates (blue solid spheres), intermediate activity with neutral substrates (white solid spheres), and the highest activity with negative substrates (red solid spheres). The PMF accumulates positive substrates resulting in enhanced activity while completely excluding negative substrates and showing negligible activity.

encapsulating non-native macromolecular cargos. 23-25 VLPs derived from bacteriophage P22 have been explored as nanoreactors encapsulating a wide range of enzymatic cargos. 26,27 The P22 VLPs assemble from 420 coat proteins (CPs), directed by 100-300 scaffolding proteins (SPs) forming highly symmetrical 56 nm, T = 7, icosahedral particles with SP lining the interior lumen of the resulting VLPs.<sup>28</sup> Nonnative protein cargos have been genetically fused to truncated forms of SP which direct them to the interior of the capsid, while maintaining assembly characteristics. <sup>26,29</sup> The resulting concentration of macromolecules inside the VLPs closely resembles macromolecular concentrations found in cells  $(\sim 200-300 \text{ mg/mL})$ , where enzymes are frequently organized into clusters or subcompartments, which are thought to increase efficiency. The porous nature of the capsid allows diffusion of substrates of a defined size and charge across while preventing the escape of the encapsulated enzymes. 30 The P22 capsid has several well characterized morphologies, two of which are Procapsid (PC) and Expanded (EX), each exhibiting a different molecular porosity.<sup>31</sup> PC is the structure initially formed upon self-assembly, while EX particles have a 10% larger diameter and are more angular than their PC precursor, most closely resembling the morphology of the infectious phage. The effective pore sizes of PC and EX are 4.4 and 2.7, respectively, which affords a degree of control over molecular access to encapsulated enzymes.<sup>32</sup> Though not used in this work, a third morphology of P22 can be obtained upon removal of the 12 pentameric units from EX particles. This

morphology, referred to as the wiffle ball (WB), has 10 nm pores at the missing pentameric vertices.<sup>31</sup>

VLPs have been used to assemble ordered crystalline arrays by taking advantage of their exterior surface. 14,15,33-38 P22 VLPs carry a negative exterior surface charge and when mixed with positively charged polyamidoamine (PAMAM) dendrimers, below a threshold ionic strength, results in the reversible self-assembly of higher order superlattice materials with a face-centered-cubic (fcc) arrangement.<sup>39</sup> Further treatment of this superlattice with an engineered ditopic protein (DecSSDec), that binds to specific sites on the P22 capsid and bridges between neighboring particles, results in a stabilization of the lattice to form what is known as a protein macromolecular framework (PMF).40 When treated at high ionic strength, above the threshold required for superlattice assembly, the templating multivalent PAMAM dendrimers can be removed leaving a material which retains its ordered structure but with very high surface charge density. The caveat in this assembly process is that the ditopic Dec protein only binds to the EX and WB structures, not the PC. 41 Previous work described the PMF formation from WB VLP nanoreactors, which exhibited catalytic turnover rates similar to those of individual particles, implying unimpeded diffusion of substrate molecules into the PMF. 40 PMFs are conceptually similar MOFs, where both can self-assemble into ordered lattice structures in which organic linkers secure the frameworks at geometrically defined locations; PMFs consist of VLP

and protein linker building blocks, whereas MOFs incorporate metal atoms that connect the framework.

Here, we demonstrate enhanced catalytic properties in the PMFs, which result from the collective behavior of VLPs in the material and which are distinct from the behavior of free individual VLPs; whereas in our previous work with small molecule substrates, the activities observed between these two materials were very similar. Due to the relatively large interparticle distances and high charge density of the porous framework, we can selectively partition highly charged cationic macromolecules into the negatively charged PMF material. In contrast, their negatively charged counterparts are effectively excluded from the PMF lattice. Exploiting the porosity and high charge density of the framework, we also demonstrate the selective partitioning of positively charged small-molecule enzyme substrates into PMFs assembled from P22 nanoreactors, resulting in a significant enhancement of the catalytic activity over the individual P22 nanoreactors (Figure 1). The ability to selectively partition substrates into the PMF material for enhanced catalytic activity is a biocompatible and green approach to the design and construction of functional proteinbased catalyst materials. The robust PMF versatility lies in our ability to impart a desired functionality through the encapsulation of any enzyme inside individual P22 VLPs, while the interstitial space and porosity of the PMF provide room for diffusion of substrates with selectivity based on size and charge.

### **RESULTS AND DISCUSSION**

Assembly of Protein Macromolecular Framework. The protein macromolecular frameworks (PMFs) were assembled using expanded (EX) P22 VLP-nanoreactors with encapsulated alcohol dehydrogenase-D enzymes (AdhD). Individual P22 VLPs were prepared and characterized confirming that the coat protein (CP) and scaffolding protein-AdhD fusion protein (AdhD-SP) initially assembled into particles with procapsid (PC) morphology (Figure S1). SDS-PAGE analysis revealed two protein bands consistent with the CP and AdhD-SP expected molecular weights, which are 48,490 Da and 52,230 Da, respectively (Figure S1a, sequence information). The PC particles were transformed into the expanded morphology (EX), which is required for formation of the PMF material, employing a method using SDS that was verified using native agarose gel electrophoresis (Figure S1e).<sup>42</sup> TEM images confirmed the expected size of the particles (64  $\pm$ 2 nm diameter) and general homogeneity of our sample (Figure S1d). These materials were further characterized by SEC-MALS, from which we could measure the molecular weight, calculate the average number of AdhD-SP cargo molecules per particle (53  $\pm$  2), and determine the particle size  $(R_g = 27.1 \pm 0.1 \text{ nm})$ . The SEC chromatograms showed a slightly earlier elution of the EX particles compared to the PC particles, and the  $R_g$  (23.1  $\pm$  0.1 nm  $\rightarrow$   $R_g$  = 27.1  $\pm$  0.1 nm) indicated the expected increase in size during morphogenesis from the PC to EX morphology (Figure S1f). The  $R_o/R_H$  ratio increased from 0.7 to 0.8 indicating that the EX particles have fewer cargo molecules, an observation consistent with previous work. 42 Mass spectrometry results showed the expected molecular weight for the CP subunits confirming that no undesired protein cleavage took place during expansion (Figure S2).

EX particles were assembled into a well-ordered lattice through the addition of a branched polymer, polyamidoamine

(PAMAM) dendrimer, at 208 mM ionic strength (I). The P22dendrimer lattice was further stabilized by the addition of the ditopic protein linker, made from the dimerization of DecS134C and referred to as DecSSDec (Figures S1 and S2), which bound to and bridged the exterior of EX particles. SAXS analysis of the initial array showed an organization consistent with an fcc lattice, and upon addition of the ditopic DecSSDec, the lattice parameter increased from a = 92.6 nm to a = 97.7 nm, calculated using SAXS peaks shifting from Q =  $0.0115 \text{ Å}^{-1}$  to Q =  $0.0111 \text{ Å}^{-1}$  (PMF SAXS can be found in Figure S1g). This indicates that the order of the assembly was retained but with an increase in interparticle distances. The G6 dendrimers were then removed from the framework by incubating and washing the framework with high ionic strength (I = 508 mM) buffer. The retention of SAXS peaks and their location suggested that the order was preserved upon removal of the G6 dendrimers, as shown in Figure S1g. Overall, the SAXS data showed that the EX P22- AdhD particles assembled into the expected fcc PMF structure, allowing us to further explore the functionality of this material.<sup>40</sup>

Partitioning of Charged Macromolecules into the PMF. After removal of the structure templating PAMAM dendrimer, the PMF was dialyzed into a lower ionic strength buffer (I = 43 mM). Under these conditions, incubation of the PMF with charged macromolecules resulted in the selective partitioning of positively charged species into the PMF material, while excluding those that are negatively charged. The pI of the CP is 4.91, while the DecS134C has a pI of 5.33, and we thus anticipated that at pH 7.0 all the components of the PMF would be negatively charged. This was verified by measuring the zeta potentials of all components (Table S4) and is consistent with the templating and binding of the initial positively charged PAMAM dendrimers. As a direct result of this, the assembled PMFs have a microenvironment that is different from the individual noninteracting P22 nanoreactors in the bulk, referred to as P22<sub>free</sub>. We expect that the PMF material is highly permeable as previously demonstrated and by estimation of the available void volume. 39,40 Even though P22 VLPs are arranged in an fcc structure, they are not closepacked, and thus, we calculate that the total volume of a P22 fcc unit cell is  $9.33 \times 10^5$  nm<sup>3</sup> with 58.8% VLP occupancy. Additionally, 45.5% of the volume of the VLP is available to solvent ( $\sim 1.06 \times 10^5 \text{ nm}^3/\text{VLP}$ ). The Dec molecules can also occupy between  $1.25 \times 10^4$  nm<sup>3</sup> and  $1.67 \times 10^4$  nm<sup>3</sup> of the unit cell based on the 60 high-affinity and 20 low-affinity sites (80 sites total) available for DecSSDec binding on the exterior of the VLPs. Considering Dec and P22 VLPs in the lattice, roughly 39% of the interstitial volume and ~85% of the total unit cell volume is available to solvent. The highly negatively charged PMF material should result in Coulombic interactions with positively charged species and potentially partition these species into the PMF while excluding equivalent negatively charged species. To test this hypothesis, four different studies were undertaken: a) partitioning of G1-G6 and G0.5-G5.5 PAMAM dendrimers into the PMF analyzed using SAXS, b) partitioning of supercharged GFP proteins (+ and -) into the PMF analyzed by fluorescence, c) partitioning of small G0.5 and 1.5 PAMAM dendrimers, modified by the conjugation of NADH (NADH- $_{x}^{y}$ ), into the PMF analyzed by the absorbance characteristics of the NADH, and d) the functional effects of the NADH-xy partitioning of the activity of the PMF as compared to P22<sub>free</sub> nanoreactors.

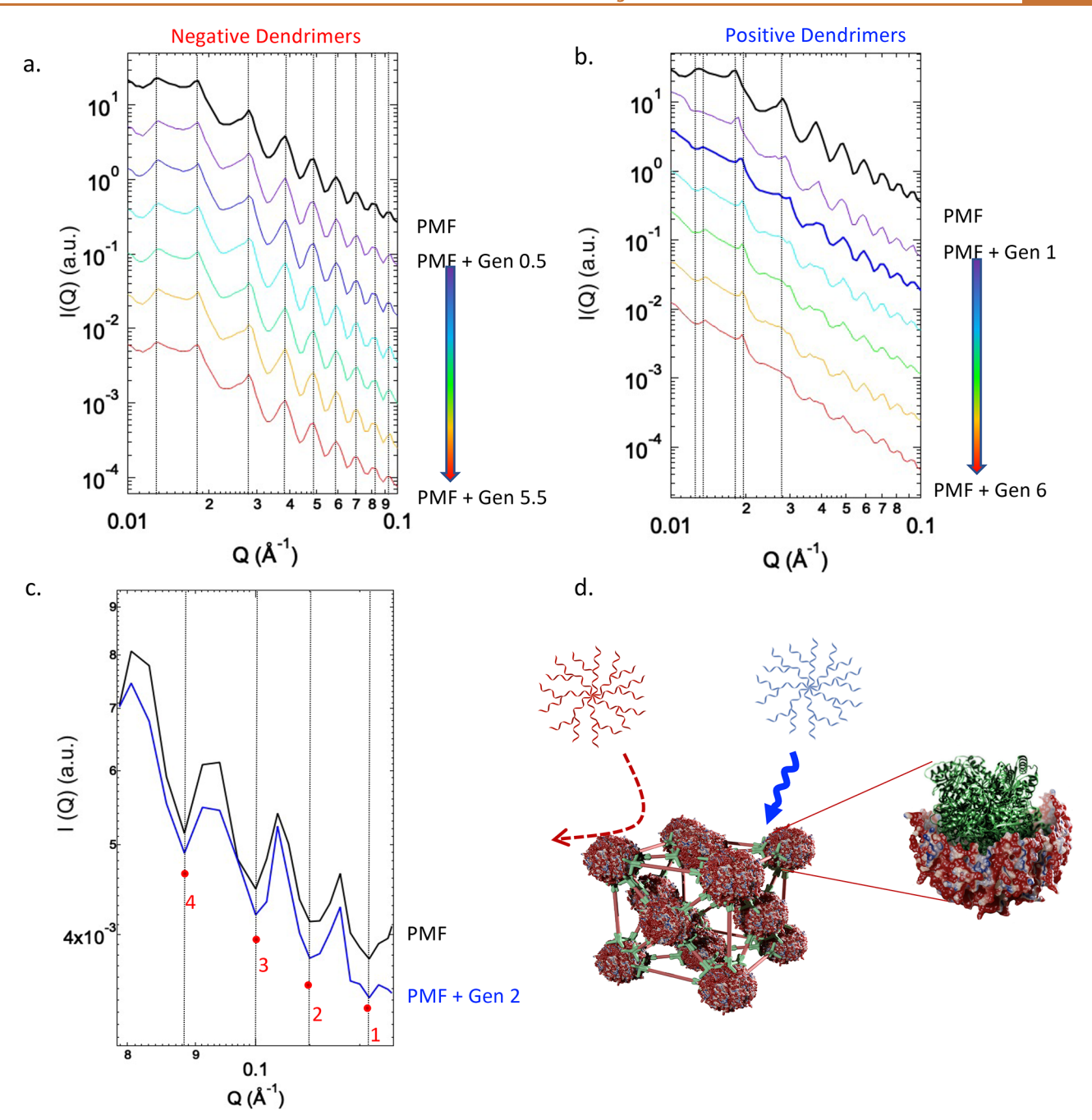


Figure 2. SAXS analysis of the PMF with G1-6 or G0.5-5.5. The PMF trace (black) is used as a control to compare with the scattering after the introduction of (a) negative dendrimers—G0.5-5.5 and (b) positive dendrimers—G1-6. The vertical lines are guides to show any shifts of the characteristic peaks, and the rainbow coloring depicts increasing dendrimer generations in accordance with the arrow. (c) Magnified view of the high Q regions of the two highlighted traces in (b) the PMF and PMF+G2. The circles denote the peak minima regions that were compared in our analysis, while the numbers refer to arbitrarily assigned peak numbers. (d) Cartoon illustrating positively charged dendrimers entering the PMF, while the negative dendrimers are excluded.

Partitioning of PAMAM Dendrimers into the PMF. Both positive (G1-G6) and negative dendrimers (G0.5-G5.5) were introduced to the PMF, and their accumulation or exclusion was monitored using SAXS (Figure 2). As expected, the negatively charged dendrimers, ranging from 2.2 nm to 6.7 nm in diameter with 8–256 charged surface groups, showed almost complete exclusion from the framework, indicated by the lack of measurable changes to the structure and form factors (Figure 2a). On the other hand, there were changes in each scattering profile upon addition of the positively charged dendrimers to the PMF material (PMF + G1-G6) shown in

Figure 2b. The peak minima at  $Q \approx 0.1 \text{ Å}^{-1}$  for the PMF (black) and PMF+G2 (blue) were used as representative examples to calculate shifts in particle size (Figure 2c). Peak minima 1–4 were identical for the two profiles–0.122, 0.11, 0.1, and 0.08833 Å<sup>-1</sup>, revealing that the particle size likely did not change upon addition of G2. Interestingly, a peak shift was observed from  $Q_{\rm PMF}=0.01817 \text{ Å}^{-1}$  to  $Q_{\rm PMF+G2}=0.01875 \text{ Å}^{-1}$ , suggesting a slight contraction or collapse of the lattice back to the original size before the addition of DecSSDec. These values equate to a decrease of the lattice constant (a) and interparticle distance (D) from  $a_{\rm PMF}=97.7 \text{ nm}$  to  $a_{\rm PMF+G2}=92.6 \text{ nm}$  and

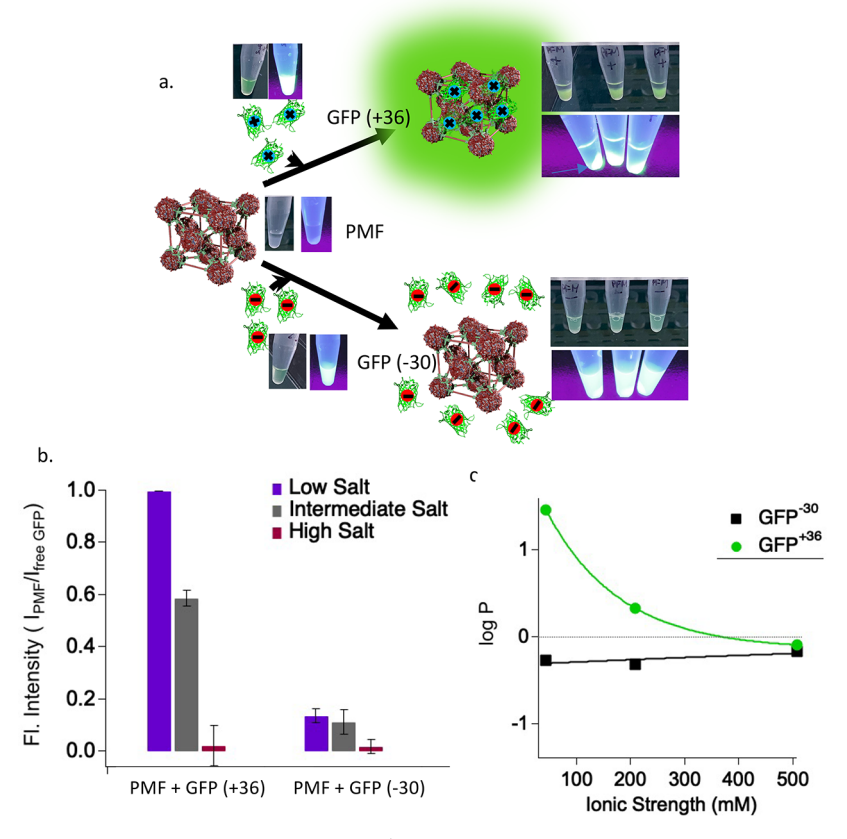


Figure 3. Analysis of the PMF with supercharged GFP (GFP<sup>+36</sup> and GFP<sup>-30</sup>). (a) Cartoon schematic alongside photographs acquired throughout the experiment where fluorescent GFP (GFP<sup>+36</sup> or GFP<sup>-30</sup>) was introduced to the nonfluorescent PMF. The GFP<sup>+36</sup> partitioned into the framework, resulting in a green pellet in the suspended phase (top image) and condensed phase (bottom image). The GFP<sup>-30</sup> was excluded from the PMF, and the green coloring can be seen dispersed in solution in the suspended phase (top image) and the condensed phase (bottom image). (b) Quantitative analysis of GFP ratios of  $\text{GFP}_{\text{PMF}}$ :GFP $_{\text{free}}$  using a fluorescence signal in different salt conditions where the corresponding ionic strengths are low salt (LS) = 43 mM, intermediate salt (IS) = 208 mM, and high salt (HS) = 508 mM. (c) The log of the calculated partition coefficient (P) for GFP<sup>+36</sup> (green) and GFP<sup>-30</sup> (black) versus the ionic strength in each buffer condition. The gray line indicates zero on the y-axis.

from  $D_{PMF}$  = 69 nm to  $D_{PMF+G2}$  = 65 nm. We attribute these changes to a decrease in interparticle spacing resulting from the partitioning of G2 molecules acting as multivalent counterions which reduce repulsive electrostatic interactions between the P22 VLPs within the lattice. The peak shifted further upon the addition of G3 to  $Q_{PMF+G3} = 0.01934 \text{ Å}^{-1}$  and remained constant for G3-G6. The gradual peak shift is likely because G3 dendrimers have more charged groups, compared to G1-2, and thus screen repulsive interactions between the VLPs more effectively. Beyond G3, the interparticle distance does not decrease likely because the minimum distance has been achieved, and indeed the  $D_{PMF+G3} = 62$  nm is consistent with the expected size of P22 VLPs. An alternative explanation for the gradual shift could be due to the small G1 being distributed between the interior cavity of P22 and the interstitial space of the PMF, and with increasing dendrimer generations, the access to the VLP interior is inhibited; thus, the larger dendrimers reside exclusively in the interstitial space.<sup>32</sup> Although it is not possible to identify the location of the dendrimers based on these data, the GFP data in the next section and these SAXS data together suggest that positively charged polymers partition into the PMF and interact with the P22 VLPs in that environment, while the negatively charged molecules are completely excluded from the PMF lattice (Figure 2d).

**Partitioning of Supercharged GFP into the PMF.** To exploit the charge dependent partitioning, we demonstrated that the PMF can selectively partition the superpositively charged macromolecule,  $GFP^{+36}$ , while excluding its negatively charged counterpart,  $GFP^{-30}$  (Figure 3). The PMF was incubated with either  $GFP^{+36}$  or  $GFP^{-30}$  in buffer solutions with I=43 mM, 208 mM, or 508 mM, and after removal of the PMF, the supernatants were recovered, and the fluorescence and absorbance measurements were measured (Figure 3a,b and Figures S3–S5). The  $GFP^{(\pm)}$  molar quantities introduced to the PMF were based on previously established values of G6 per P22 particle for PC and WB fcc lattices, and an approximate charge equivalent was used here.

As expected, at I=43 mM, most GFP<sup>+36</sup> molecules diffused into the PMF and can be seen from the fluorescent pellet and clear supernatant in the images (Figure 3a and Figure S3). No fluorescence or absorbance signatures characteristic of GFP were detected in the recovered supernatant. We calculate that  $\sim 406$  GFP<sup>+36</sup> per P22 VLP partitioned into the lattice, corresponding to 1624 GFP<sup>+36</sup> per unit cell. This value suggests that there was approximately 1 GFP<sup>+36</sup> per CP subunit. Fewer GFPs<sup>+36</sup> partitioned into the PMF as the ionic strength was increased (Figure 3b and Figures S3–S5), where at I=208 mM there were  $\sim 231$  GFP<sup>+36</sup>/P22 VLP (or 924 per unit cell). At I=508 mM, there was almost no difference

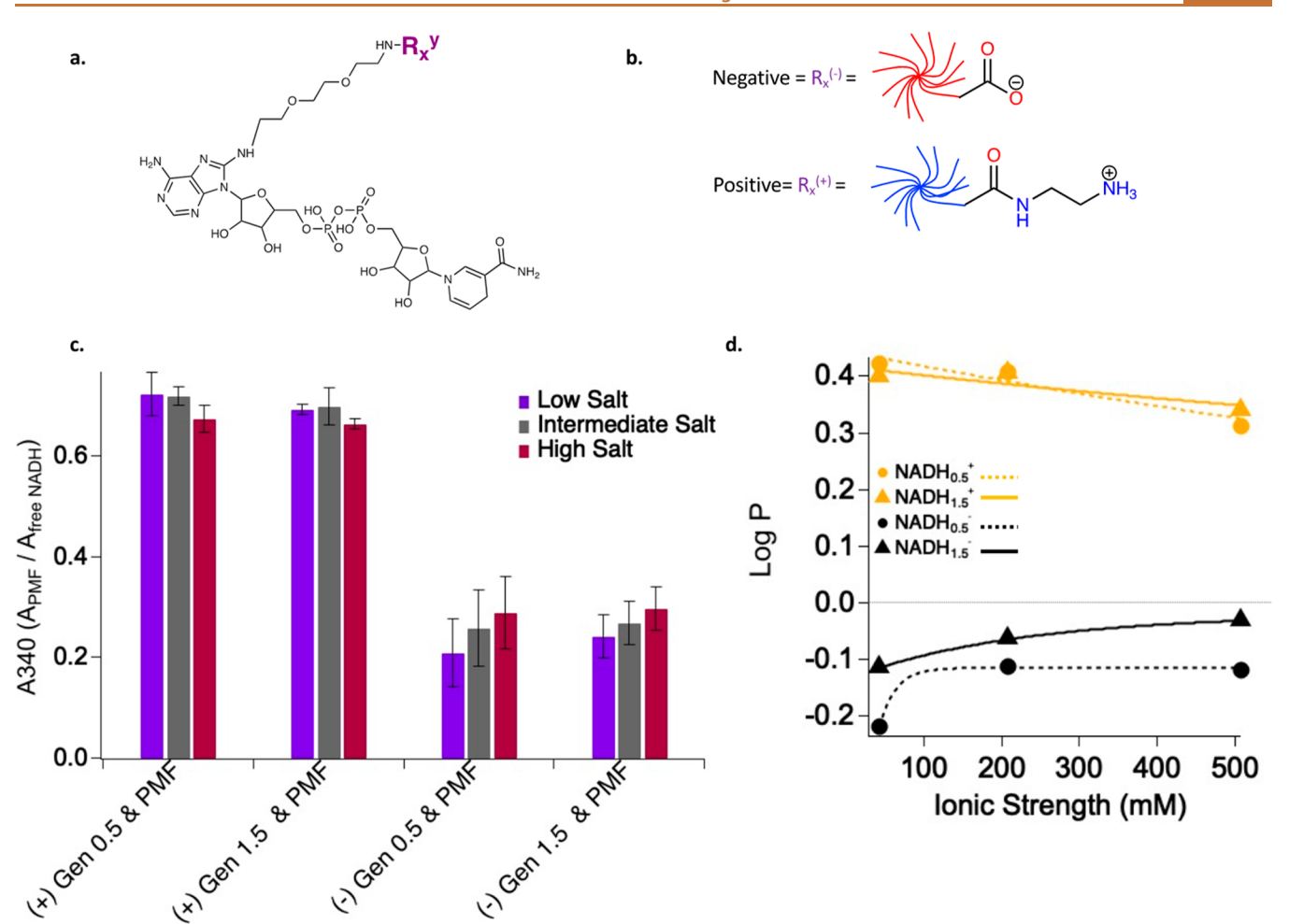


Figure 4. Analysis of the PMF with NADH<sub>x</sub><sup>y</sup>. (a) The chemical structure of the modified NADH molecule with an  $R_x$  where x refers to the dendrimer generation (0.5 or 1.5) and y refers to the overall charge of the molecule (+, 0, – stand for positive, neutral, and negative, respectively). (b) Cartoon of the positive dendrimer with terminal primary amine groups and a negative dendrimer with terminal carboxylate groups rendering their respective charges. (c) Absorbance ratios for NADH<sub>x</sub><sup>y</sup><sub>PMF</sub>:NADH<sub>x</sub><sup>y</sup><sub>free</sub> in different salt conditions where the corresponding ionic strengths are low salt = 43 mM, intermediate salt = 208 mM, and high salt = 508 mM. (c) The log of the calculated partition coefficient (P) for NADH<sub>x</sub><sup>+</sup> (yellow) and NADH<sub>x</sub><sup>-</sup> (black) versus the ionic strength in each buffer condition. The gray line indicates zero on the y-axis.

between the GFP<sup>+36</sup> concentration before and after incubation with the PMF due to charge screening effects in the high salt (HS) conditions. There was no ionic strength dependence on the exclusion of GFPs<sup>-30</sup> from the PMF, shown by the images where the fluorescence is dispersed throughout the sample in all conditions (Figure 3a and Figures S3 and S4). Measurement of the absorbance and fluorescence of the solution before and after removal of the PMF showed no difference, indicating exclusion of the negative GFP even in high ionic strength conditions.

We then used this as a model system to evaluate the distribution of molecules between the supernatant and the PMF and calculated the partition coefficient (P)

$$Log P = Log \left( \frac{[GFP_{PFM}]}{[GFP_{Sup}]} \right)$$

where [GFP<sub>PMF</sub>] is the concentration of either GFP<sup>-30</sup> or GFP<sup>+36</sup> remaining in the framework, and [GFP<sub>Sup</sub>] is the concentration recovered from the supernatant. While P typically describes the distribution of solutes in two immiscible

solvents, here we apply it to measure the ability of GFP variants to partition from the bulk solution into the PMF.

Higher P values indicate more effective distribution of the GFP molecules from the bulk solution into the framework: log P > 0 suggesting preferential transfer into the PMF, log P = 0values result from an equal distribution of molecules between the two 'phases', and  $\log P < 0$  reflects a poor diffusivity into the framework and therefore a preference for the bulk solution. The GFPs<sup>+36</sup> have P > 0 values for I = 43 and 208 mM and P =-0.09 for I = 508 indicating that while the former conditions successfully partition the GFPs+36 into the framework, the latter are close to equally distributed between the phases. A similar exponential decrease is observed in the calculations of the Debye length (SI calculations).  $GFP^{-30}$  displayed a preference for the bulk solution with negative log P values at all I and approaching zero with increasing I. With these data, we show that by using electrostatic interactions in the PMF we can control the distribution of charged biomacromolecules within these materials.

Partitioning of NADH Conjugated PAMAM Dendrimers into the PMF. Using a previously established protocol for synthesizing NADH conjugates, we made and

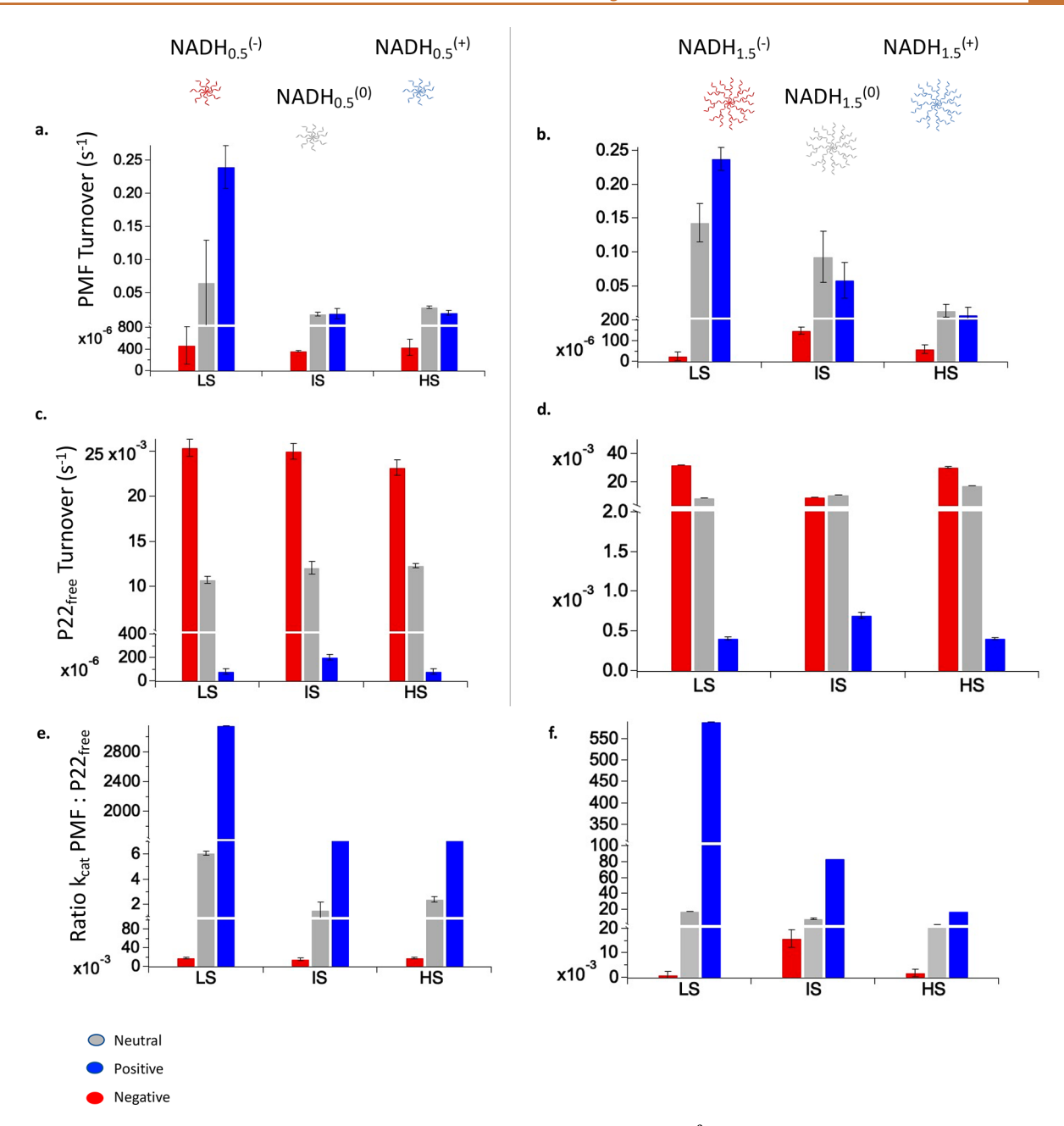


Figure 5. Catalytic activity of the PMF with charged substrates.  $NADH_{x}^{+} = blue$ ,  $NADH_{x}^{0} = gray$ ,  $NADH_{x}^{-} = red$ . All the bar graphs on the left correspond to  $NADH_{0.5}^{y}$ , and those on the right correspond to  $NADH_{1.5}^{y}$ . (a,b) Turnover values ( $k_{cat}$ ) for the PMF with  $NADH_{0.5}^{y}$  and  $NADH_{1.5}^{y}$  in low salt (LS), intermediate salt (IS), and high salt (HS). (c,d) Turnover values for  $NADH_{0.5}^{y}$  and  $NADH_{1.5}^{y}$  in  $P22_{free}$ . (e,f) Ratio of  $k_{cat}$  for the PMF: $P22_{free}$  using  $NADH_{0.5}^{y}$  and  $NADH_{1.5}^{y}$ , respectively.

characterized Generation 0.5 and 1.5 polyamidoamine (PAMAM)—NADH conjugates with either negative or positive terminal groups: NADH $_{0.5}$ <sup>(-), (+)</sup> and NADH $_{1.5}$ <sup>(-), (+)</sup> (Figure 4). <sup>32,43</sup> We previously determined the EX P22 pore size to be 2.7 nm, and the dendrimer modified substrates chosen for this work were therefore below this size threshold to ensure the substrates could access the enzymes encapsulated on the interior of the P22 VLPs. NADH is a cofactor required for AdhD-catalyzed reactions, and its characteristic absorbance at 340 nm provided a straightforward way to quantify the partition coefficient of these molecules into the PMF. The absorbances for NADH $_{0.5}$ <sup>(-), (+)</sup> and NADH $_{1.5}$ <sup>(-), (+)</sup> before and after incubation with the PMF can be found in Figure S6, while the ratios of molecules partitioning into the lattice versus those

remaining free in solution (ratio PMF:free NADH) are found in Figure 4c,d. NADH<sub>0.5, 1.5</sub> (-) did not partition into the framework, and the log P values remained negative for all ionic strength conditions, albeit approaching log P=0 with increasing ionic strength. This was expected because as the Debye length decreases (because of increasing I) some NADH<sub>0.5, 1.5</sub> (-) can likely get into the interior of the P22 particles. On the other hand, the NADH<sub>0.5, 1.5</sub> (+) molecules display preferential partitioning into the PMF at all ionic strengths (P=2.0-2.6), with the highest P values at I=43 mM (P=2.6). The NADH<sub>0.5, 1.5</sub> (-) and NADH<sub>0.5, 1.5</sub> (+) molecules display similar trends for charge dependent partitioning into the PMF as the GFP<sup>-30</sup> and GFP<sup>+36</sup> but are affected differently by the ionic strength. This can be seen by

comparing NADH<sub>0.5, 1.5</sub><sup>(+)</sup> and GFP<sup>+36</sup>, where log  $P \approx 0$  at I = 508 mM for GFP<sup>+36</sup>, while NADH<sub>0.5, 1.5</sub><sup>(+)</sup> maintains preference for partitioning into the PMF. This is most likely due to the ability of the positively charged NADH conjugates to diffuse into the interior cavity of P22 nanoreactors in addition to occupying the interstitial space of the lattice, while GFP variants can only access the interstitial spaces. Based on previously reported simulation and experimental data, <sup>44</sup> we expect that the charged macromolecules can sample the available space, exchange with bulk solvent, and avoid being locked into defined positions within the lattice in all ionic strength conditions used in these studies.

Catalytic Protein Macromolecular Framework Material. To fully realize the potential of this material, we show that the ionic strength-dependent partitioning effect increases the local concentration of charged substrates within the PMF resulting in a dramatic enhancement of enzyme activity compared to noninteracting individual VLP nanoreactors in bulk solution (Figure 5).

Monitoring AdhD enzyme kinetics using NADH<sub>x</sub><sup>(+)</sup> substrates (Figure S7c), we observed activity in the PMF that was 2800× and 550× faster than those observed with NADH<sub>0.5</sub><sup>(+)</sup> and NADH<sub>1.5</sub><sup>(+)</sup> with free individual P22 VLPs, respectively (Figure 5). This was in stark contrast to our previously reported activity where the P22 VLPs and the PMF material exhibited similar reaction rates when unconjugated NADH was used as a substrate.<sup>40</sup> This observation suggests that the differences in activity measured in this study are due to the highly charged dendrimers and that the charges on NADH alone are not sufficient to alter the partitioning and reaction rates. When considering the ionic strength dependence of  ${\rm NADH_{0.5}}^{(+)}$  and  ${\rm NADH_{1.5}}^{(+)}$  on PMF enzyme activity, we saw the highest activity at 43 mM followed by a considerable decline at 208 and 508 mM (Figure 5a/b). The accelerated reaction rates can be attributed to the partitioning of NADH, (+) into the PMF resulting in a higher local concentration of NADH substrates ([NADH<sub>x</sub><sup>(+)</sup>] in the PMF =  $\sim$ 1.4 mM). At very low ionic strengths (I = 0), the dendrimers have previously been modeled to be bound tightly and essentially irreversibly to the P22 building blocks.<sup>45</sup> However, at slightly elevated ionic strength (where "low salt" experiments were performed-43 mM), they partition into the lattice but remain mobile enough to allow them to diffuse across the P22 capsid and access the VLP encapsulated enzyme. In contrast, experiments with individual P22<sub>free</sub> VLPs showed low activity with NADH<sub>x</sub><sup>(+)</sup>, likely due to a balance between electrostatic attraction between the negatively charged VLPs and the NADH<sub>0.5 and 1.5</sub><sup>(+)</sup> ( $\zeta$  = 12 mV and 14 mV), and repulsive interactions with the electrostatic gradient through the pore (Figure 5c/d).<sup>32</sup> Interestingly, we did not see a pronounced dependence on ionic strength for the  $P22_{free}$  activity with  $NADH_x^{(+)}$ , which remained low in all salt conditions. It is likely that repulsive interactions dominate at all ionic strengths because the Debye length at 508 mM (4.3 Å) still exceeds the narrowest distance between inner-pore residues (1.5 Å), which we modeled in previous work.<sup>32</sup> It is likely that the high local concentration of NADH<sub>x</sub><sup>(+)</sup> partitioned within the PMF can overcome any repulsive interactions in the pore seen with P22<sub>free</sub> and result in the observed enhanced catalytic activity. To ensure that we were closely mimicking the P22 VLPs found within the PMF, the kinetics were measured on EX P22<sub>Dec</sub>-AdhD VLPs, which are individual noninteracting P22 VLPs that have the wtDec

proteins bound to the exterior of the VLP. Given these differences between the PMF and P22<sub>free</sub>, it appears that a previously unattained property emerges in the PMF, where the collective electrostatic field far exceeds that of individual P22 VLPs.

When the  $NADH_x^{(-)}$  molecules were introduced to the PMF, the enzyme activity was measured to be negligible at all ionic strengths. As an example, at 43 mM, the  $k_{\rm cat}$  values were 4.6E-4 s<sup>-1</sup> and 2.5E-5 s<sup>-1</sup> (Figure S8 and Tables S2 and S3) for NADH<sub>0.5</sub> (-) and NADH<sub>1.5</sub> (-), respectively, while the  $k_{\rm cat}$  values for P22<sub>free</sub> with NADH<sub>0.5</sub> (-) and NADH<sub>1.5</sub> (-) were 0.025 s<sup>-1</sup> and 0.032 s<sup>-1</sup>, respectively, comparable to values previously reported (Figure S7 and Tables S2 and S3).32 At this ionic strength (43 mM), the Debye length of 1.59 nm allows, or aids, NADH, (-) passage across the individual P22 pores, but the negative PMF material excludes NADH,  $^{(-)}$  from the interstitial spaces therefore limiting access of these negatively charged NADH substrates to the P22 pores and the encapsulated enzymes. We increased the ionic strength to 508 mM, decreasing the theoretical Debye length to 0.43 nm, to assess the screening of the repulsive electrostatic interactions (Figure 5a/b and Figure S7). The turnover values obtained with the PMF increased slightly to 4.3E-4 s<sup>-1</sup> and 5.8E-4 s<sup>-1</sup> for  $NADH_{0.5}^{(-)}$  and  $NADH_{1.5}^{(-)}$ , respectively. This was still well below the activity exhibited with individual P22<sub>free</sub> which was like the activity measured at 208 mM ionic strength. These results were consistent with our observations of exclusion of  ${\rm GFPs^{-30}}$  and  ${\rm NADH_{0.5,\ 1.5}}^{(-)}$  from the PMF, where even at high ionic strength, the negative macromolecules do not appear to have access to the PMF.

Neutral NADH substrates (NADH<sub>0.5, 1.5</sub><sup>(0)</sup>) whose zeta potentials lie between NADH<sub>0.5, 1.5</sub><sup>(-)</sup> and NADH<sub>0.5, 1.5</sub><sup>(+)</sup> were also evaluated. At I=43 mM (low salt (IS)), the molecular charge largely governs PMF enzyme activity, and the turnover rates of the NADH<sub>0.5, 1.5</sub><sup>(0)</sup> molecules lie between the two oppositely charged NADH molecules. At intermediate salt (IS) and high salt (HS) conditions, the activity of NADH<sub>0.5, 1.5</sub><sup>(0)</sup> became more comparable to NADH<sub>0.5, 1.5</sub><sup>(+)</sup> and overall showed a lower dependence on ionic strength than either of the charged substrates. The activity of P22<sub>free</sub> with NADH<sub>0.5, 1.5</sub><sup>(0)</sup> also remained relatively consistent across the three salt conditions. These molecules provided additional support for our hypothesis and underlined the interplay of ionic strength and substrate charge on enzyme activity.

The differences in kinetic behavior between  $P22_{\text{free}}$  and the PMF were most pronounced when we analyzed the turnover rates as a ratio of the PMF:P22<sub>free</sub> (Figure 5e/f). This highlights the electrostatic contribution of substrate partitioning and the difference between the behavior of the PMF and the free P22 nanoreactors. The  $k_{\rm cat}$  ratios of the PMF:P22 $_{\rm free}$  for NADH $_{0.5}^{(+)}$  and NADH $_{1.5}^{(+)}$  are 2800 and 550, respectively, at I = 43 mM and reflect the complete reversal of the substrate charge dependence of the PMF and the P22<sub>free</sub>. Differences between the  $NADH_{0.5}^{(+)}$  and  $NADH_{1.5}^{(+)}$  are due to the smaller molecules having a lower turnover rate with P22<sub>free</sub> likely due to the shorter length of dendrimer branches and their lowered ability to sample the interior of the VLPs. These data support our hypothesis that the turnover rate of the catalytic PMF can be tuned using a combination of solvent ionic strength and electrostatic characteristics of the substrates. Furthermore, these data suggest that our engineered nanoreactor systems exhibit properties within the PMF very

different from those of individual VLPs, resulting in the ability to preferentially partition substrates into the PMF.

### **CONCLUSIONS**

The use of enzymes for synthetic catalysts can benefit from immobilization on a support material, generating a heterogeneous catalyst material that facilitates recovery and reuse. Here, we show the construction of a biodegradable protein-only macromolecular framework material (PMF) serving as a heterogeneous catalyst with pronounced selectivity and drastically higher activity than its homogeneous counterpart. We report that our protein framework assembles into extended materials, and this heterogeneous phase can selectively accumulate positively charged fluorescent biomacromolecules, such as GFP+36, while excluding those that are negative (GFP<sup>-30</sup>), resulting in a high partition coefficient. Similarly, the PMF can preferentially partition a modified enzyme substrate (NADH), typically used as a cofactor in many enzymatic reactions. By carefully tuning the ionic strength, the positive substrates can reach a much higher local concentration in the interstitial space in the PMF and within the P22 particles encapsulating the AdhD enzymes in the PMF. By monitoring the enzyme activity, we show that the PMF is highly selective for positive substrates, while the individual P22<sub>free</sub> are selective toward negative ones, which can be further tuned with different ionic strength conditions. This demonstrates a complete reversal of the substrate charge dependence of the PMF and P22<sub>free</sub>. What was most intriguing was that the assembly of P22<sub>free</sub> into the PMF material showed collective behavior where PMF activity was at least 10× higher than the fastest P22<sub>free</sub> activity in this study and 2800× higher when comparing the positively charged substrates. This work demonstrates that biological building blocks can be used to construct heterogeneous catalysts with tunable properties, such as small molecule partitioning and rates of catalyst activity, using a combination of substrates charge and ionic strength. This is a step toward designing hierarchically assembled protein-based catalytic materials with adjustable and userdefined properties. We envision that this methodology can be extended to tune the activity of other enzymes and even exploit other noncovalent interactions, such as hydrophobicity, to selectively concentrate substrates in the catalytic phase.

# METHODS AND EXPERIMENTAL SECTION

Protein Preparation. P22. A dual vector expression system was used in which pRSF Duet (MS2) and pBAD contained the coat protein (CP) and scaffolding protein fused to alcohol dehydrogenase enzyme-D (AdhD-SP), respectively.<sup>45</sup> The P22 CP was genetically modified to include Ecoil-2x peptide-((VAALEKE)<sub>2</sub>) at the Cterminus, which has previously been shown to promote the formation of more ordered lattices.<sup>39</sup> The SP used here is a truncated variant (residues 142-303), with AdhD fused to the N-terminal end. Kanamycin (Kan) and ampicillin (Amp) genes were added to pRSF Duet and pBAD, respectively, to maintain selection for the plasmids. Both plasmids were simultaneously transformed into BL21 electrocompetent E. coli cells and, after screening colonies, were grown at 37 °C in the presence of both antibiotics (30  $\mu$ g/mL and 50  $\mu$ g/mL for Kan and Amp, respectively). AdhD-SP expression was induced with Larabinose (13.3 mM final concentration) when cells reached mid log phase (OD<sub>600</sub> = 0.5–0.8) and continued incubation for 4 h at 37  $^{\circ}$ C. CP expression was induced with isopropyl  $\beta$ -D-thiogalactopyranoside (IPTG-0.5 mM final concentration) and continued growing overnight at room temperature. The cells were harvested via centrifugation (4,500 × g, 10 min, 4 °C), and pellets were resuspended in a buffer (pH 7.0, 50 mM sodium phosphate, 100

mM sodium chloride) in the presence of Pierce Protease Inhibitor tablets and frozen at  $-80\,^{\circ}\text{C}$ . The cells were thawed and treated with an enzyme cocktail containing DNase, RNase, and lysozyme for 30 min at room temperature. To further assist in cell lysis, the suspension was sonicated and centrifuged to remove cell debris (12,000  $\times$  g, 45 min, 4 °C). The supernatant was recovered and further purified via ultracentrifugation through a 35% (w/v) sucrose cushion (215,619  $\times$  g, 50 min, -4 °C) . The pellets were resuspended in the same buffer as mentioned above for lysis and further purified over Sephacryl-500 using Biorad Duoflow FPLC. The fractions collected were pooled, and protease inhibitor was added for storage to mitigate cleavage of the Ecoil-2x peptide. All extinction coefficients were calculated using the ExPASy ProtParam tool.

wtDec and DecS134C. A pET Duet vector was used for both wtDec and DecS134C genes with 6xHis-tags to assist in later purification steps. <sup>46</sup> An ampicillin (Amp) gene was added to the vectors to maintain selection for the plasmids. Plasmids were separately transformed into BL21 electrocompetent *E. coli* cells and, after screening colonies, were grown at 37 °C in the presence of antibiotic Amp–50 μg/mL. Protein expression was induced with isopropyl β-D-thiogalactopyranoside (IPTG–0.5 mM final concentration) when cells reached mid log phase (OD<sub>600</sub> = 0.5–0.8) and continued incubation overnight at 37 °C. The cells were removed *via* centrifugation (4,500 × g, 45 min, 4 °C), and supernatant was recovered. The supernatant was filtered and applied to a 5 mL Roche cOmplete His-Tag purification column on a Biorad Duoflow FPLC. The respective proteins were eluted using a 20–500 mM imidazole gradient, and fractions were pooled and dialyzed into phosphate buffer.

Reduction and Oxidation of DecS134C. DecS134C is highly susceptible to post-translational modification via S-glycosylation and therefore needed to be reduced to increase yield and availability of thiols for the formation of DecS134C dimer. Reduction was performed by incubating DecS134C protein (1 mg/mL) in phosphate buffer with 5 mM dithiothreitol (DTT) for 3 h at room temperature followed by overnight dialysis back into the phosphate buffer. The oxidation of DecS134C to form disulfide dimers (DecSSDec) proceeded via incubation of the reduced DecS134C with 20  $\mu$ M copper(II) sulfate (CuSO<sub>4</sub>) overnight at 4 °C and heating at 60 °C for 20 min. It was common for a precipitate to form after this step and was removed prior to dialysis back to standard phosphate buffer.

P22 Characterization. SEC-MALS. P22 VLP concentration was adjusted to 1 mg/mL, and size-exclusion chromatography coupled with multiangle light scattering (SEC-MALS) was used to determine the radius and molecular weight of the particles. The sample was injected using Agilent 1200 HPLC and separated using WTC-200S 5 μM, 2000 Å, 7.8 × 300 mm column. A 16-angle MALS detector (HELEOS-Wyatt Technology Corporation) and an Optilab rEX refractometer (Wyatt Technology Corporation) determined the molecular weight (M) by using eq 1 in Astra 5.3.14 software (Wyatt Technology Corporation). The dn/dc is 0.1850 mL/g and is the known refractive index increment for protein material.  $R(\theta)$  is the excess Rayleigh ratio from solute,  $n_0$  is the solvent refractive index,  $N_A$  is Avogadro's number,  $\lambda_0$  is the wavelength of incident light, c is the solute concentration in w/v, and  $P(\theta)$  is the form factor.

$$M = \frac{R(\theta)}{\frac{4\pi^2 n_0^2}{N_A \lambda_0^4} \left(\frac{\mathrm{d}n}{\mathrm{d}c}\right)^2 c P(\theta)}$$
(1)

TEM. Transmission electron microscopy (TEM) was used to determine the size of the particles and overall quality of the samples. The samples were prepared at 0.2 mg/mL concentation in phosphate buffer, and 10  $\mu$ L was loaded onto glow-discharged Formvar coated grids. The droplet was incubated for 5 min and wicked away using filter paper. The grid was washed by adding 10  $\mu$ L of water and incubating for 5 min. After removing the water droplet, 10  $\mu$ L of 1% (v/v) uranyl acetate was deposited onto the grid. After a 5-min incubation, the uranyl acetate was wicked away, using a Kimwipe to remove any remaining liquid. JEOL TEM instrumentation was used to image the particles at an accelerating voltage of 100 kV.

Native Agarose Gel Shift Assay. A 0.8% (w/v) agarose gel was prepared using 50 mL of 40 mM Tris (pH 8.2), 5 mM acetate, and 1 mM EDTA. A loading buffer was added to a protein sample (1 mg/mL, 10  $\mu$ L), and the shift assay was run at 75 V for 2 h using Tris (above) as the running buffer. The gel was incubated with Instablue for 1 h and water overnight. The image was taken using a UVP MultDoc-IT Digital Imaging System.

Expansion of P22 Using SDS. Using a previously established methodology, a fresh solution of 0.2% (7 mM) sodium dodecyl sulfate (SDS) was prepared and added to an equal volume of 1 mg/mL P22 PC solution, both in a solution (pH 7.0, 50 mM sodium phosphate, 100 mM sodium chloride). <sup>42</sup> Incubation proceeded for 5 min, and ultracentrifugation (2×) removed SDS and any broken particles. The native agarose shift assay and SEC-MALS were used to confirm, and the resulting particles were expanded.

PMF Assembly and Characterization. A solution containing EX P22 VLPs (1 mg/mL) was prepared in a buffer (pH 7.0, 50 mM sodium phosphate, 100 mM sodium chloride). In order to assemble the lattice, a fresh solution of PAMAM generation 6 (G6) dendrimers was prepared in a 1:4 dilution in the same buffer as above and added slowly, with gentle mixing, to the solution containing P22 VLPs in a 1000-fold excess of dendrimers per particle, which is well above the required amount.<sup>39</sup> The solution became turbid immediately, indicating that the VLPs and G6 have coalesced. The condensed phase was allowed to settle at room temperature before addition of the protein linker. The DecS134C-protein linker was prepared in the same buffer, and the concentration was adjusted to 2 mg/mL. The P22-G6 lattice was gently mixed, and the DecS134C solution was added in a 160:1 molar ratio of trimeric linker:P22 VLPs. 40 There are 80 total binding sites, resulting in a 2:1 Dec trimer to P22 binding site ratio. This solution was kept at room temperature for 30 min and stored overnight at 4 °C. In order the remove the dendrimer, the samples were gently centrifuged (5,000 × g, 3 min, 4 °C), and the supernatant was removed leaving a small white pellet at the bottom of the tube. The pellet was resuspended in a buffer (pH 7.0, 50 mM sodium phosphate, 400 mM sodium chloride) by pipetting and centrifuged again (5,000 × g, 3 min, 4 °C). This step was repeated twice to ensure that all dendrimers were removed from the PMF. The PMF was then centrifuged and resuspended into a buffer (pH 7.0, 50 mM sodium phosphate, 100 mM sodium chloride) until further use. For experiments performed in low and high ionic strength buffers (pH 7.0, 10 mM sodium phosphate, 20 mM sodium chloride and pH 7.0, 50 mM sodium phosphate, 400 mM sodium chloride, respectively), the PMF was resuspended into respective buffers via similar wash steps immediately prior to the experiments.

SAXS Analysis. All samples were adjusted to a 1 mg/mL P22 concentration and in a buffer (pH 7.0, 50 mM sodium phosphate, 100 mM sodium chloride), unless otherwise stated. The control samples— G6 dendrimer and DecS134C-were adjusted to match the contents within the framework. The buffers used for background subtraction matched the respective buffer conditions of each individual sample. All small-angle X-ray scattering (SAXS) data were collected at the Advanced Photon Source (APS) at Argonne National Laboratories, beamline 12 ID-B (14 keV). A syringe pump was used to inject the samples and continuously agitated to minimize damage and prevent sedimentation. The Pilatus 2 M detector was used to take 20 shots of each sample, that were converted from two-dimensional scattering patterns to one-dimensional curves, averaged, and background subtracted using an appropriate buffer to provide scattering intensity-I(q). The data was presented as I(q) versus the scattering vector (q), given by eq 2

$$Q = \frac{4\pi \sin \theta}{\lambda} \tag{2}$$

where  $\theta$  is half of the scattering angle, and  $\lambda$  was the wavelength used to acquire the measurements. The form factor (P(Q)) was measured separately using P22 VLPs (not assembled) in the same buffer conditions and concentrations. Structure factors (S(q)) were extracted using both I(Q) and P(Q), as previously described.

Measuring the Partition Coefficient Using Supercharged GFP Variants. The negative and positive GFP variants (GFP-30 and GFP<sup>+36</sup>, respectively) were separately exchanged into three different pH 7.0 buffer solutions—low salt (LS), normal salt (NS), and high salt (HS) where the concentrations of each were 10 mM sodium phosphate, 20 mM sodium chloride; 50 mM sodium phosphate, 100 mM sodium chloride; and 50 mM sodium phosphate, 400 mM sodium chloride. The concentrations of GFP were adjusted using absorbance at 280 nm on an Agilent Cary 8454 UV-vis Diode Array System, and the characteristic GFP absorbance at 492 nm was seen to be slightly affected by the ionic strength. The PMF was centrifuged and resuspended into the three different buffers containing either GFP<sup>-30</sup> or GFP<sup>+36</sup> and gently agitated using a pipet. As a control, the same volume and stock solution were used to measure GFP absorbance before incubation with the PMF. The condensed phase was settled, and the supernatant was recovered and measured after centrifugation. All absorbance and fluorescence measurements of the supernatant were taken using a BioTek Cytation 5 Cell Imaging Multi-Mode Reader. The number of GFP variants partitioning into the framework was measured and calculated using two different methods-1) measuring the absorbance of the supernatant before and after incubation with the PMF material and 2) after the supernatant was decanted, the PMF was resuspended in high salt buffer to remove the partitioned molecules from the framework, and absorbance was measured again. Both methods yielded comparable results. To estimate the number of GFP molecules per unit cell, we considered the input concentration of P22 VLPs upon framework assembly and used that value to determine the number of VLPs per PMF sample. For example, if 100  $\mu$ L at 45 nM P22 concentration was used for the PMF assembly and no measurable protein was removed during the subsequent wash steps, then we estimated that at constant volume the [P22 VLP] was 45 nM.

Measuring the Partition Coefficient Using NADH Variants.  $NADH_{0.5}^{(-),(+)}$  and  $NADH_{1.5}^{(-),(+)}$  concentrations were adjusted using NADH characteristic absorbance at 340 nm. Equal volumes of each were added to the three different buffer conditions used for the GFP variants—LS, NS, and HS—and added to the PMF pellet using gentle agitation. The condensed phase was settled, and the supernatant was recovered and measured after centrifugation. All absorbance measurements of the supernatant were taken using a BioTek Cytation 5 Cell Imaging Multi-Mode Reader.

Monitoring Enzyme Activity of P22 VLPs and the PMF. The concentrations of P22 VLPs were adjusted to reach a final concentration of 650 nM encapsulated AdhD-SP in the three different buffer conditions-LS, NS, and HS, while the PMF was adjusted to contain 1 mg/mL P22 VLPs. To avoid the presence of free enzymes, resulting from the escape of broken particles, the samples were passed over a Ni-NTA column, which allowed for the removal of any free His-tagged AdhD-SP enzymes. P22 VLPs were exchanged into respective buffers using ultracentrifugation (215,619 × g, 50 min, -4 °C), and the PMF was exchanged using gentle centrifugation (5,000 × g, 3 min, 4 °C). Acetoin was prepared in the three different buffers with concentrations ranging from  $\hat{1}$  to 120 mM. NADH<sub>0.5</sub> (-), (+) and  $NADH_{1.5}^{(-), (+)}$  were prepared in water at high concentrations to prevent oxidation of NADH during dialysis. Typically, the NADH variants were added to the reaction vials in a 1:100 dilution, resulting in negligible changes to the buffer concentrations. The final concentrations of NADH ranged from 160  $\mu$ M to 220  $\mu$ M ( $\varepsilon_{340}$  =  $6.22\ mM^{-1}\ cm^{-1})$ . It is possible that the extinction coefficients are different for the modified NADH molecules, and since we are primarily looking at the differences in activity between P22 VLPs and the PMF, this difference is neglected. Seven different concentrations of acetoin were used, with an eighth sample containing no acetoin and measuring oxidation of NADH used for background subtraction. The kinetics of P22 VLP AdhD-SP were monitored using a BioTek Cytation 5 Cell Imaging Multi-Mode Reader by adding 5  $\mu$ L using the instrument's autoinject function, agitating for 1 min, and using kinetics mode function to monitor absorbance at 340 and 600 nm. The 600 nm wavelength was monitored to determine if there was aggregation within the sample over the course of the kinetics run. To

monitor the kinetics of the PMF, 8 different stock solutions were prepared containing the PMF (@ 1 mg/mL P22 VLPs), NADH variant, and acetoin (of varying concentrations). To prevent excessive centrifugation, the supernatants from 8 solutions were aliquoted for the following time points: 3, 6, 9,15, 21, 30, 60, and 120 min and constantly agitated to prevent the PMF from settling. Upon reaching each individual time point, the respective aliquots were centrifuged (17,000  $\times$  g, 1 min), the supernatant was recovered, and the supernatant absorbance measurements were taken using the plate reader. This was repeated a minimum of three times for each condition. The Michaelis—Menten kinetics model (eq 3) was using to extract the Michaelis—Menten constant ( $K_{\rm M}$ ) and the turnover rate ( $k_{\rm cat}$ ). The concentration of the enzyme was determined using absorbance at 280 nm, and the MW values were determined by SEC-MALS, as previously described.

$$f(C) = \frac{\nu[C]}{K_{\rm m} + [C]} \tag{3}$$

Synthesis of NADH<sub>0.5</sub><sup>(-), (-), (0)</sup> and NADH<sub>1.5</sub><sup>(-), (+), (0)</sup>. 8-NAD<sup>+</sup>-Br. As previously described, NAD<sup>+</sup> (1.00 g, 1.5 mmol) was dissolved in 500 mM sodium acetate buffer (pH 4.5, 20 mL) at room temperature.<sup>32</sup> The solution was stirred vigorously as bromine (0.4 mL, 7.8 mmol) was added slowly and dropwise to the stirring solution through a septum under argon. The reaction was typically complete after 4 h but can be left overnight. The reaction was then added to a separatory funnel, and excess unreacted bromine was removed using chloroform. The extraction was complete when the organic layer was clear, and the aqueous layer was a pale yellow. The aqueous layer was recovered and dialyzed into water using 500 MW cutoff cellulose dialysis tubing (Spectrum Laboratories) for 48 h. The product was lyophilized and stored until the next step (0.606 g, 55% yield). <sup>1</sup>H NMR (400 MHz, D<sub>2</sub>O)  $\delta$  9.25 (s, 1H), 9.10 (d, 1H), 8.75 (d, 1H), 8.20 (t, 1H), 8.1 (s, 1H), 6.10 (d, 1H), 5.95 (d, 1H), 4.0–4.5 (m, 9H).

8-NADH-Br. Argon gas was bubbled through 1.3% (v/w) sodium bicarbonate buffer (155 mM, 15 mL) for 1 h, after which 8-NAD+-Br (303 mg, 0.420 mmol) was dissolved and blanketed with argon. Sodium dithionite was added to the solution (150 mg) and stirred under argon gas for 4 h. The solution turned a bright yellow color upon addition of the reducing agent and gradually faded throughout the course of the reaction. To ensure than all available 8-NAD+-Br has been reduced, another equivalent of sodium dithionite was added and monitored over the next hour. The reaction was complete when the absorbance at 256 and 340 nm had a 3:1 ratio or when the ratio remained the same over time. The argon line was removed, and the solution was stirred while exposed to air for 30 min. The product was precipitated using a 10× volume of cold acetone. A pellet was collected, resuspended in water, and lyophilized. <sup>1</sup>H NMR (400 MHz,  $D_2O$ )  $\delta$  8.1 (s, 1H), 6.82 (s, 1H), 6.18 (d, 1H), 5.80 (d, 1H), 4.0-5.0 (m, 11H), 2.9 (m, 2H).

8-NADH-NH<sub>2</sub>. 8-NADH-Br (0.3 g) was dissolved in 6 mL of DMSO by heating to 60 °C and blanketed with argon gas. The linker, 2,2'-(ethylenedioxy)bis(ethylamine), was dissolved in DMSO in a separate vial (1.285 g, 8.32 mmol) and added to the heated solution containing 8-NADH-Br. The resulting mixture was stirred at 80 °C for 2 h or 60 °C for 6 h (both options result in similar yields) and then at room temperature overnight. The product was recovered as a beige solid after precipitating with 10× volume of cold acetone. <sup>1</sup>H NMR (400 MHz, D<sub>2</sub>O)  $\delta$  8.2 (s, 1H), 6.75 (s, 1H), 5.85–6.10 (m, 2H), 5.25 (dd, 1H), 3.8–4.5 (m, 9H), 3.1–3.5 (m, 13H), 2.80 (d, 2H) 1.01 (t, 1H).

 $8\text{-NADH}_x^{(-)}$ . Carboxyl-terminated PAMAM dendrimer generations 0.5 and 1.5 (G0.5 and G1.5, respectively) were used for the following synthesis in which either G0.5 or G1.5 was dissolved in 3 mL of 100 mM MES buffer (pH 4.7) with EDC in a 10-fold excess of 8-NADH-NH<sub>2</sub>. To that solution was added 8-NADH-NH<sub>2</sub> (25 mg, 30.8  $\mu$ mol) such that the stoichiometric ratio of NADH:G0.5 was 1, and for NADH:G1.5, the stoichiometric ratio was 2. The solution was stirred overnight and then dialyzed into water using cellulose dialysis tubing.

 $8\text{-NADH}_x^{(0)}$ . To neutralize the charge on the dendrimers,  $8\text{-NADH}_x^{(-)}$  was dissolved in 3 mL of 100 mM MES buffer (pH 4.7) with EDC in a 10-fold excess of the terminal carboxylate group. The dendrimer concentration was approximated to be that of the previous step, and NADH concentration was measured using absorbance at 340 nm. To that solution was added an equimolar ratio (to EDC) of methyl amine, and the mixture was stirred overnight. Dialysis was used to remove an unreacted methyl amine, and the charge neutralization was verified using zeta potential measurements.

 $8\text{-NADH}_x^{(+)}$ . To reverse the charge of the dendrimers,  $8\text{-NADH}_x^{(-)}$  was dissolved in 3 mL of 100 mM MES buffer (pH 4.7) with EDC in a 10-fold excess of the terminal carboxylate group. The dendrimer concentration was approximated to be that of the previous step, and NADH concentration was measured using absorbance at 340 nm. In a separate vial, an equimolar amount (to EDC) of ethylenediamine was dissolved in 3 mL of the same buffer. The solution turned warm upon addition. Once the solution cooled, it was added to the solution containing  $8\text{-NADH}_x^{(-)}$  and stirred overnight. Dialysis was used to remove any unreacted ethylenediamine, and the charge reversal was verified using zeta potential measurements.

# **ASSOCIATED CONTENT**

# Supporting Information

The Supporting Information is available free of charge at https://pubs.acs.org/doi/10.1021/acsnano.1c05004.

Supplemental amino acid sequences of all proteins used in this work, tables containing information about proteins (pI, molecular weight), calculations, information on modified dendrimers (hydrodynamic radii, zeta potential measurements), and acquired Michaelis Menten values ( $K_{\rm M}$ ,  $k_{\rm cat}$ ), uncropped gel images presented in main figures, full MS spectra, raw data values collected using PMF + GFP<sup>(±)</sup>, raw data values collected using PMF and NADH<sub>x</sub><sup>y</sup>, and Michaelis Menten plots collected using P22<sub>free</sub> and PMF (PDF)

# **AUTHOR INFORMATION**

# **Corresponding Author**

Trevor Douglas — Department of Chemistry, Indiana University, Bloomington, Indiana 47405, United States; orcid.org/0000-0002-7882-2704; Phone: 812-856-6936; Email: trevdoug@iu.edu

### Authors

Ekaterina Selivanovitch — Department of Chemistry, Indiana University, Bloomington, Indiana 47405, United States

Masaki Uchida — Department of Chemistry and Biochemistry, California State University Fresno, Fresno, California 93740, Unites States; orcid.org/0000-0003-0710-8834

Byeongdu Lee — X-ray Science Division, Advanced Photon

Source, Argonne National Laboratory, Argonne, Illinois 60439, United States; o orcid.org/0000-0003-2514-8805

Complete contact information is available at: https://pubs.acs.org/10.1021/acsnano.1c05004

### Notes

The content is solely the responsibility of the authors and does not necessarily represent the official views of the National Institutes of Health.

The authors declare no competing financial interest.

### **ACKNOWLEDGMENTS**

This work was funded by a grant from the Human Frontier Science Program (HFSP) 4124801. E.S. was partially

supported by the Graduate Training Program in Quantitative and Chemical Biology under Award T32 GM109825 and Indiana University. T.D. was supported in part by the National Science Foundation through grant 1720625. M.U. was in part supported by the National Science Foundation grant CMMI-1922883. SAXS data was collected at Beamline 12-ID-B, Advanced Photon Source, Argonne National Laboratory. We thank the IU Electron Microscopy Center, the Nanoscale Characterization Facility, and the Physical Biochemistry Instrumentation Facility for access to their instrumentation.

### **REFERENCES**

- (1) Johnson, C. W. What Are Emergent Properties and How Do They Affect the Engineering of Complex Systems? *Reliability Engineering and System Safety* **2006**, *91* (12), 1475–1481.
- (2) Aksyuk, A. A.; Rossmann, M. G. Bacteriophage Assembly. *Viruses* **2011**, 3 (3), 172–203.
- (3) Juhl, S. B.; Chan, E. P.; Ha, Y. H.; Maldovan, M.; Brunton, J.; Ward, V.; Dokland, T.; Kalmakoff, J.; Farmer, B.; Thomas, E. L. Assembly of Wiseana Iridovirus: Viruses for Colloidal Photonic Crystals. *Adv. Funct. Mater.* **2006**, *16* (8), 1086–1094.
- (4) Barthelat, F.; Yin, Z.; Buehler, M. J. Structure and Mechanics of Interfaces in Biological Materials. *Nat Rev Mater* **2016**, *1* (4), 16007.
- (5) Fratzl, P.; Weinkamer, R. Nature's Hierarchical Materials. *Prog. Mater. Sci.* **2007**, *52* (8), 1263–1334.
- (6) Meyers, M. A.; McKittrick, J.; Chen, P.-Y. Structural Biological Materials: Critical Mechanics-Materials Connections. *Science* **2013**, 339 (6121), 773–779.
- (7) Sen, D.; Buehler, M. J. Structural Hierarchies Define Toughness and Defect-Tolerance Despite Simple and Mechanically Inferior Brittle Building Blocks. *Sci. Rep.* **2011**, *1*, 35.
- (8) Brodin, J. D.; Carr, J. R.; Sontz, P. A.; Tezcan, F. A. Exceptionally Stable, Redox-Active Supramolecular Protein Assemblies with Emergent Properties. *Proc. Natl. Acad. Sci. U. S. A.* **2014**, *111* (8), 2897–902.
- (9) Buchberger, A.; Simmons, C. R.; Fahmi, N. E.; Freeman, R.; Stephanopoulos, N. Hierarchical Assembly of Nucleic Acid/Coiled-Coil Peptide Nanostructures. *J. Am. Chem. Soc.* **2020**, *142* (3), 1406–1416.
- (10) Grindy, S. C.; Learsch, R.; Mozhdehi, D.; Cheng, J.; Barrett, D. G.; Guan, Z.; Messersmith, P. B.; Holten-Andersen, N. Control of Hierarchical Polymer Mechanics with Bioinspired Metal-Coordination Dynamics. *Nat. Mater.* **2015**, *14* (12), 1210–6.
- (11) Bartlett, P.; Campbell, A. I. Three-Dimensional Binary Superlattices of Oppositely Charged Colloids. *Phys. Rev. Lett.* **2005**, 95 (12), 128302.
- (12) Han, K.; Bailey, J. B.; Zhang, L.; Tezcan, F. A. Anisotropic Dynamics and Mechanics of Macromolecular Crystals Containing Lattice-Patterned Polymer Networks. *J. Am. Chem. Soc.* **2020**, *142* (45), 19402–19410.
- (13) Heater, B. S.; Yang, Z.; Lee, M. M.; Chan, M. K. *In Vivo* Enzyme Entrapment in a Protein Crystal. *J. Am. Chem. Soc.* **2020**, 142 (22), 9879–9883.
- (14) Korpi, A.; Anaya-Plaza, E.; Valimaki, S.; Kostiainen, M. Highly Ordered Protein Cage Assemblies: A Toolkit for New Materials. *Wiley Interdiscip. Rev.: Nanomed. Nanobiotechnol.* **2020**, 12 (1), No. e1578.
- (15) Korpi, A.; Ma, C.; Liu, K.; Nonappa; Herrmann, A.; Ikkala, O.; Kostiainen, M. A. Self-Assembly of Electrostatic Cocrystals from Supercharged Fusion Peptides and Protein Cages. *ACS Macro Lett.* **2018**, *7* (3), 318–323.
- (16) Sato, O. Dynamic Molecular Crystals with Switchable Physical Properties. *Nat. Chem.* **2016**, *8* (7), 644–56.
- (17) Selivanovitch, E.; Douglas, T. Virus Capsid Assembly across Different Length Scales Inspire the Development of Virus-Based Biomaterials. *Curr. Opin. Virol.* **2019**, *36*, 38–46.
- (18) Schoonen, L.; Van Hest, J. C. Compartmentalization Approaches in Soft Matter Science: From Nanoreactor Development to Organelle Mimics. *Adv. Mater.* **2016**, 28 (6), 1109–1128.

- (19) Wang, G.; Kuroda, K.; Enoki, T.; Grosberg, A.; Masamune, S.; Oya, T.; Takeoka, Y.; Tanaka, T. Gel Catalysts That Switch on and Off. *Proc. Natl. Acad. Sci. U. S. A.* **2000**, 97 (18), 9861–9864.
- (20) Hawkins, K.; Patterson, A. K.; Clarke, P. A.; Smith, D. K. Catalytic Gels for a Prebiotically Relevant Asymmetric Aldol Reaction in Water: From Organocatalyst Design to Hydrogel Discovery and Back Again. *J. Am. Chem. Soc.* **2020**, *142* (9), 4379–4389.
- (21) Li, D.; Xu, H.-Q.; Jiao, L.; Jiang, H.-L. Metal-Organic Frameworks for Catalysis: State of the Art, Challenges, and Opportunities. *EnergyChem* **2019**, *1* (1), 100005.
- (22) Zhao, M.; Ou, S.; Wu, C.-D. Porous Metal-Organic Frameworks for Heterogeneous Biomimetic Catalysis. *Acc. Chem. Res.* **2014**, *47* (4), 1199–1207.
- (23) Douglas, T.; Young, M. Host-Guest Encapsulation of Materials by Assembled Virus Protein Cages. *Nature* **1998**, 393 (6681), 152–155.
- (24) Steinmetz, N. F.; Lim, S.; Sainsbury, F. Protein Cages and Virus-Like Particles: From Fundamental Insight to Biomimetic Therapeutics. *Biomater. Sci.* **2020**, 8 (10), 2771–2777.
- (25) Schwarz, B.; Uchida, M.; Douglas, T. Biomedical and Catalytic Opportunities of Virus-Like Particles in Nanotechnology. *Adv. Virus Res.* **2017**, *97*, 1–60.
- (26) O'Neil, A.; Reichhardt, C.; Johnson, B.; Prevelige, P. E.; Douglas, T. Genetically Programmed *in Vivo* Packaging of Protein Cargo and Its Controlled Release from Bacteriophage P22. *Angew. Chem., Int. Ed.* **2011**, *50* (32), 7425–8.
- (27) Patterson, D. P.; Prevelige, P. E.; Douglas, T. Nanoreactors by Programmed Enzyme Encapsulation inside the Capsid of the Bacteriophage P22. ACS Nano 2012, 6 (6), 5000–5009.
- (28) King, J.; Botstein, D.; Casjens, S.; Earnshaw, W.; Harrison, S.; Lenk, E. Structure and Assembly of the Capsid of Bacteriophage P22. *Philosophical Transactions of the Royal Society of London. B, Biological Sciences* **1976**, 276 (943), 37–49.
- (29) Parker, M. H.; Casjens, S.; Prevelige, P. E., Jr Functional Domains of Bacteriophage P22 Scaffolding Protein. *J. Mol. Biol.* **1998**, 281 (1), 69–79.
- (30) McCoy, K.; Selivanovitch, E.; Luque, D.; Lee, B.; Edwards, E.; Caston, J. R.; Douglas, T. Cargo Retention inside P22 Virus-Like Particles. *Biomacromolecules* **2018**, *19* (9), 3738–3746.
- (31) Teschke, C. M.; McGough, A.; Thuman-Commike, P. A. Penton Release from P22 Heat-Expanded Capsids Suggests Importance of Stabilizing Penton-Hexon Interactions during Capsid Maturation. *Biophys. J.* **2003**, *84* (4), 2585–2592.
- (32) Selivanovitch, E.; LaFrance, B.; Douglas, T. Molecular Exclusion Limits for Diffusion across a Porous Capsid. *Nat. Commun.* **2021**, *12* (1), 2903.
- (33) Suci, P. A.; Klem, M. T.; Arce, F. T.; Douglas, T.; Young, M. Assembly of Multilayer Films Incorporating a Viral Protein Cage Architecture. *Langmuir* **2006**, 22 (21), 8891–8896.
- (34) Aumiller, W. M.; Uchida, M.; Douglas, T. Protein Cage Assembly across Multiple Length Scales. *Chem. Soc. Rev.* **2018**, 47 (10), 3433–3469.
- (35) Cigler, P.; Lytton-Jean, A. K.; Anderson, D. G.; Finn, M. G.; Park, S. Y. DNA-Controlled Assembly of a NaTl Lattice Structure from Gold Nanoparticles and Protein Nanoparticles. *Nat. Mater.* **2010**, *9* (11), 918–22.
- (36) Strable, E.; Johnson, J. E.; Finn, M. Natural Nanochemical Building Blocks: Icosahedral Virus Particles Organized by Attached Oligonucleotides. *Nano Lett.* **2004**, *4* (8), 1385–1389.
- (37) Chung, W. J.; Oh, J. W.; Kwak, K.; Lee, B. Y.; Meyer, J.; Wang, E.; Hexemer, A.; Lee, S. W. Biomimetic Self-Templating Supramolecular Structures. *Nature* **2011**, *478* (7369), 364–8.
- (38) Liljeström, V.; Mikkilä, J.; Kostiainen, M. A. Self-Assembly and Modular Functionalization of Three-Dimensional Crystals from Oppositely Charged Proteins. *Nat. Commun.* **2014**, *5* (1), 4445.
- (39) Uchida, M.; McCoy, K.; Fukuto, M.; Yang, L.; Yoshimura, H.; Miettinen, H. M.; LaFrance, B.; Patterson, D. P.; Schwarz, B.; Karty, J. A.; Prevelige, P. E., Jr.; Lee, B.; Douglas, T. Modular Self-Assembly of

- Protein Cage Lattices for Multistep Catalysis. ACS Nano 2018, 12 (2), 942-953.
- (40) McCoy, K.; Uchida, M.; Lee, B.; Douglas, T. Templated Assembly of a Functional Ordered Protein Macromolecular Framework from P22 Virus-Like Particles. *ACS Nano* **2018**, *12* (4), 3541–3550.
- (41) Schwarz, B.; Madden, P.; Avera, J.; Gordon, B.; Larson, K.; Miettinen, H. M.; Uchida, M.; LaFrance, B.; Basu, G.; Rynda-Apple, A. Symmetry Controlled, Genetic Presentation of Bioactive Proteins on the P22 Virus-Like Particle Using an External Decoration Protein. ACS Nano 2015, 9 (9), 9134–9147.
- (42) Selivanovitch, E.; Koliyatt, R.; Douglas, T. Chemically Induced Morphogenesis of P22 Virus-Like Particles by the Surfactant Sodium Dodecyl Sulfate. *Biomacromolecules* **2019**, *20* (1), 389–400.
- (43) Kraj, P.; Selivanovitch, E.; Lee, B.; Douglas, T. Polymer Coatings on Virus-Like Particle Nanoreactors at Low Ionic Strength-Charge Reversal and Substrate Access. *Biomacromolecules* **2021**, 22 (5), 2107–2118.
- (44) Brunk, N. E.; Uchida, M.; Lee, B.; Fukuto, M.; Yang, L.; Douglas, T.; Jadhao, V. Linker-Mediated Assembly of Virus-Like Particles into Ordered Arrays *via* Electrostatic Control. *ACS Appl Bio Mater* **2019**, 2 (5), 2192–2201.
- (45) Sharma, J.; Douglas, T. Tuning the Catalytic Properties of P22 Nanoreactors through Compositional Control. *Nanoscale* **2020**, *12* (1), 336–346.
- (46) Uchida, M.; LaFrance, B.; Broomell, C. C.; Prevelige, P. E., Jr.; Douglas, T. Higher Order Assembly of Virus-Like Particles (VLPs) Mediated by Multi-Valent Protein Linkers. *Small* **2015**, *11* (13), 1562–70.